Synchrotron x-rays and condensed matter/Rayonnement X synchrotron et matière condensée

Resonant Inelastic X-ray Scattering: From band mapping to inter-orbital excitations

Jan Lüning *, Coryn Frank Hague

Laboratoire de chimie physique – matière et rayonnement (UMR 7614), université Pierre et Marie Curie, 11 rue Pierre et Marie Curie, 75231 Paris cedex 05, France

Available online 31 October 2007

Abstract

Resonant inelastic X-ray scattering (also known as resonant X-ray Raman spectroscopy when only valence and conduction states are involved in the final state excitation) has developed into a major tool for understanding the electronic properties of complex materials. Presently it provides access to electron excitations in the few hundred meV range with element and bulk selectivity. Recent progress in X-ray optics and synchrotron radiation engineering have opened up new perspectives for this powerful technique to improve resolving power and efficiency. We briefly present the basics of the method and illustrate its potential with examples chosen from the literature. ***To cite this article: J. Lüning, C.F. Hague, C. R. Physique 9 (2008).***
© 2007 Académie des sciences. Published by Elsevier Masson SAS. All rights reserved.

Résumé

Diffusion X Inélastique Résonante. La diffusion X inélastique résonante, que l'on nomme aussi spectroscopie Raman X résonante lorsqu'elle met en jeu des états de valence et de conduction seuls dans l'état final, est devenue un outil majeur pour l'étude des propriétés électroniques de matériaux complexes. Actuellement la résolution de la technique se limite à quelques centaines de meV mais avec sélectivité chimique et une faible sensibilité aux effets de surface. Des progrès récents en optique X et en techniques de production du rayonnement synchrotron ouvrent de nouvelles perspectives pour cette spectroscopie puissante en améliorant le pouvoir résolvant et l'efficacité instrumentale. Nous présentons brièvement les bases de la méthode et nous l'illustrons au moyen d'exemples sélectionés de la litérature. ***Pour citer cet article : J. Lüning, C.F. Hague, C. R. Physique 9 (2008).***
© 2007 Académie des sciences. Published by Elsevier Masson SAS. All rights reserved.

Keywords: RIXS; X-ray inelastic scattering; Electron correlations

Mots-clés : RIXS ; Diffusion X inélastique ; Corrélations électroniques

1. Introduction

Resonant Inelastic X-ray Scattering (RIXS) is one of the experimental techniques that can most benefit from the high brightness provided by the insertion device beam lines of today's third generation synchrotron radiation facilities. The relative importance of this rather novel experimental technique is reflected in the installation of branch lines, specifically tailored for RIXS and equipped with dedicated end stations, at many 3rd generation synchrotron radiation

---

* Corresponding author.
 E-mail addresses: Jan.Luning@upmc.fr (J. Lüning), Hague@ccr.jussieu.fr (C.F. Hague).

facilities. Thus a presentation of the capabilities of this experimental technique has its place in this special issue of the C. R. Physique. To fulfill this goal we present an introductory overview of the properties of RIXS most readily applicable by a broad community of potential users. More detailed information can be found in the original papers or review articles we have listed [1–6] and the references therein.

We will mainly focus on excitations falling into the 'soft' part of the X-ray photon energy spectrum ($\sim$30–2000 eV) where details of the electronic structure are not concealed by the lifetime broadening of the excited core-hole state. Soft X-ray emission (SXE) spectroscopy involving the radiative transition of a valence electron or core electron into a more tightly bound core-electron vacancy, was widely used for studying the electronic structure of atoms, molecules, and solids up to the late 1960s, following on the work of H.W.B. Skinner [7]. Its importance faded with the advent of photoemission spectroscopy [8], which offers not only much higher count rates but also superior energy resolution. A revival of SXE spectroscopy occurred in the early 1990s with the arrival of undulator-insertion-device-based synchrotron radiation sources. Their smaller spot size and higher monochromatic flux density counteracts the grating spectrometer's small transmission function and intrinsically low emission decay rates. Spectroscopy with higher energy resolution and unprecedented definition of the energy of the initial core hole state of the emission was facilitated enabling element selective, resonant excitation [9] processes.

Experiments performed to-date have underlined the importance of improving spectrometer throughput and energy resolution. Several of the leading groups in the field have been encouraged to design a new generation of X-ray spectrometer thanks to progressive improvements in the performance of light sources. A brief overview of current spectrometer developments is given at the end of this article.

Within the established 'absorption-followed-by-emission' interpretation of the underlying processes it came as a surprise to observe variations in the emission spectra when the energy of the X-ray photons was stepped through the threshold region of an absorption resonance [10]. Such spectral changes were observed for atoms and molecules as well as for solids exhibiting electron–electron correlation effects or even broad valence band materials with negligible correlation effects.

The importance of these experiments came with the realization that the traditional two-step 'absorption-followed-by-emission' interpretation is generally not appropriate, but that the process has to be regarded as a one-step resonant inelastic scattering event [11]. This implies that energy and momentum conservation does not only apply to the individual absorption and emission process taken separately but is preserved through the entity of the inelastic scattering process. The differential cross section for this process is given by the Kramers–Heisenberg equation [12]:

$$\frac{d\sigma}{d\omega_2\,d\Omega} \propto \frac{\omega_2}{\omega_1} \sum_f \left| \frac{e^2}{2mc^2} \langle f|\mathbf{A}_2 \cdot \mathbf{A}_1|i\rangle \right.$$

$$\left. + \frac{e}{mc} \sum_m \left\{ \frac{\langle f|\mathbf{A}_2 \cdot \mathbf{p}_2|m\rangle\langle m|\mathbf{A}_1 \cdot \mathbf{p}_1|i\rangle}{E_m - E_i - \hbar\omega_1 - i\Gamma_m/2} + \frac{\langle f|\mathbf{A}_1 \cdot \mathbf{p}_1|m\rangle\langle m|\mathbf{A}_2 \cdot \mathbf{p}_2|i\rangle}{E_i - E_m + \hbar\omega_2} \right\} \right|^2 \cdot \delta\big(\omega_1 - \omega_2 - (E_f - E_i)\big)$$

where $|i\rangle$ and $|f\rangle$ describe the electronic configuration of the scattering object's initial and final state with energies E_i and E_f, respectively. Conventional inelastic scattering is described by the first term, proportional to the product of the vector potential of the incoming (A_1) and scattered (A_2) photon. The other two terms depend explicitly on the energy of the incident ($\hbar\omega_1$) or scattered ($\hbar\omega_2$) photon and describe so-called 'anomalous' X-ray scattering [3]. The sum in these terms runs over all possible 'virtual intermediate' states $|m\rangle$ with energy E_m. The term in the middle is referred to as the resonant term, since in the vicinity of an absorption threshold where $\hbar\omega_1$ is close to $E_m - E_i$ its contribution is enhanced by a factor of the order of $\hbar\omega_1/\Gamma_m$. In this case the resonant term dominates over the other two and it is thus the origin of the phenomena of resonant inelastic scattering discussed in this article. As a consequence of the dominance of the resonant term a time scale is introduced into the inelastic scattering process, namely, the finite lifetime of the intermediate state. This acts as a reference time scale for other processes accompanying the core-hole excitation in the intermediate state. For example, electron delocalization [13], electron–phonon scattering [14] and symmetry breaking in molecules [15] are phenomena that have been observed experimentally in RIXS. In particular the experiments on symmetry breaking in RIXS have indicated that it is even possible to alter the reference time scale, which is generally referred to as 'setting the core-hole clock'. A discussion of this effect is beyond the scope of this article, but can be found in references [15,16] and references therein. Instead we will focus in the following sections on how RIXS can be applied to map the electronic band dispersion in broad band materials with negligible electron correlation effects, to investigate electron correlation effects in strongly correlated materials, and to suppress core-hole

lifetime broadening in X-ray absorption spectroscopy [17,18]. A brief discussion of RIXS instrumentation will close the article.

2. Band structure mapping

When electron–electron correlation effects are negligible and a single electron description of the electronic structure of a material is applicable the RIXS process can be visualized in a band structure diagram as indicated in Fig. 1. In the inelastic scattering process, the change from the incident photon energy $\hbar\omega_{in}$ to the scattered photon energy $\hbar\omega_{out}$, corresponds to a change in the electronic configuration from the ground state to a valence band (VB) to conduction band (CB) excitation (for simplicity we utilize a semiconductor notation to indicate the occupied (VB) and unoccupied (CB) part of the valence structure). Since in addition to energy, momentum is also conserved in a scattering process, the momentum of the CB-electron VB-hole pair has to match the momentum transfer of the scattered photon. Here we limit our discussion to the case of soft X-ray RIXS where the momentum transfer is generally negligible in comparison to the electron momentum within the first Brillouin zone. This implies that the CB-electron and VB-hole carry the same crystal momentum (modulo a reciprocal lattice vector), a conclusion put forward initially by Ma et al. in 1992 [19].

One further notices in Fig. 1 that the energy of the incident photon controls the momentum of the CB electron. Right at the absorption threshold, where $E_{in} = \hbar\omega_{in} = E_{CBM} - E_C$, the core electron is excited into the conduction band minimum (CBM). As mentioned before the VB electron participating in the resonant inelastic scattering process has to carry the same crystal momentum. For the case of a material with an indirect band gap as indicated in Fig. 1 this implies that the energy transfer of the scattered photon is larger than the indirect band gap. Consequently, the energy of the scattered photon is smaller than the high-energy cut-off in a non-resonantly excited SXE spectrum, which corresponds to the energy of the valence band maximum (VBM)-to-core-hole transition. The electrons around the VBM can only participate in the inelastic scattering process when the excitation energy, i.e., the energy of the incident photon, is such that the core electron is excited into a CB state with a crystal momentum matching that of the VBM (k_2 in Fig. 1). The energy of the scattered photon then matches that of the high-energy cut-off in the non-resonantly excited SXE spectrum. For a direct semiconductor, on the other hand, where the CBM and VBM share the same crystal momentum, the highest scattering energy is observed right at the absorption threshold.

This difference in the inelastic scattering spectrum of a direct and an indirect band gap material is demonstrated in Fig. 2 for the case of hexagonal GaN (direct band gap) and AlN (indirect band gap) [20]. The lower spectra in each panel are the at 399.00 eV non-resonantly excited SXE spectra which in a material with negligible electron correlation effects are directly linked to the occupied part of the so-called local partial density of states (LPDOS). This is the
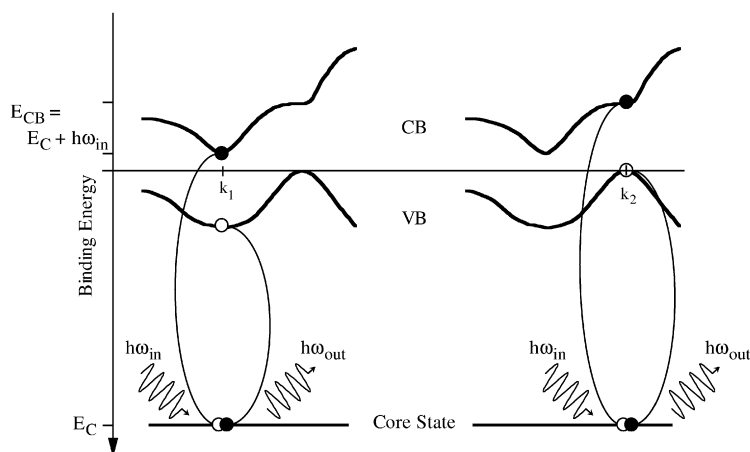

Fig. 1. Principle of RIXS within a single electron band structure picture for an indirect band gap semiconductor. Since for soft X-rays the momentum transfer is negligible, the final state consists of a vertical VB-to-CB excitation, whose crystal momentum is selected by the energy of the incoming photon as indicated.

projection of the DOS onto the wave function of the core electron (local) taking into account the angular momentum symmetry of the core electron and the photon momentum transfer in the emission process $\Delta l = \pm 1$ (partial).

The upper spectra given within each panel by the black lines are the at-threshold resonantly excited inelastic scattering spectra of GaN and AlN. In line with the above discussion the scattering peak coincides for the direct band gap material GaN with the high-energy cut-off of the non-resonantly excited SXE spectrum while for the indirect band gap material AlN the scattered intensity is located at a lower energy.

The as-measured spectra recorded in a RIXS experiment are actually those shown by the gray lines in Fig. 2, which are a superposition of the non-resonant SXE spectrum (lower black lines) and the momentum-selective RIXS spectrum (upper black lines). This indicates that for a certain fraction of inelastic scattering processes the momentum conservation is broken. Apparently the selectivity is entirely randomized over the Brillouin zone, therefore yielding a contribution equivalent to the non-resonantly excited SXE spectrum [14]. The origin of the non-k-selective part to the RIXS spectrum lies in electron–electron and electron–phonon scattering. For example, during the finite lifetime of the intermediate state these processes can yield momentum transfer to particles not directly involved in the RIXS process. The presence of such a non-k-selective fraction has been observed in all band structure mapping experiments so far (see for example Refs. [21–23]). It has also been discussed theoretically, thereby addressing also the importance of finite electron correlation effects [24]. In general, it is found that the non-k-selective fraction increases with increasing excitation energy which is in line with the increasing probability for electron–electron and electron–phonon scattering. Thus, even when using a well-defined non-resonant excitation energy high above the absorption threshold the RIXS spectrum is indeed identical to the non-resonant SXE spectrum, which traditionally was recorded using electron bombardment to create the initial core-hole vacancies. While at first the presence of this non-k-selective fraction may appear as a pure annoyance, it has been noticed that it actually enables the energy dependence of these scattering processes to be characterized experimentally [14]. As we will discuss later one also observes for materials exhibiting significant electron–electron correlation effects processes where energy or momentum is transferred to particles not directly involved in the scattering process.

For photon energies exceeding the absorption threshold the energy of the CB electron is determined by the corresponding energy difference. This, however, does not uniquely define the crystal momentum, since for any given energy above the CBM there generally exists for any given energy a 3-dimensional subset of states of the $E(k)$-landscape. Only high symmetry points of $E(k)$ have common extrema so that an energy selection at or around high symmetry points typically selects only a few k-points. In these cases RIXS data can be directly compared to band structure calculations plotted along high symmetry crystal directions and thus agreement or discrepancy between experiment and theory visualized in an intuitive way.

Fig. 3 shows the result of a study of the electronic band structure of cubic SiC as an example. The symbols indicate the peak positions extracted from RIXS spectra excited at the C K- (circle) and Si $L_{2,3}$- (squares) absorption threshold, where filled and open symbols reflect intense and weak lines, respectively. This comparison shows clearly that RIXS enables detailed band mapping of the electronic band structure. As discussed above, knowledge of the $E(k)$ relationship of the unoccupied bands is required to translate the excitation energy into crystal momentum and thus to assign the observed peaks in the RIXS spectrum to a crystal momentum.

An obvious advantage of RIXS for band structure mapping is that as an entirely photon based technique it is a true bulk probe. It is thus inherently insensitive to surface contaminations or reconstructions, which have hampered the study of the electronic band structure of SiC with angular resolved photoemission spectroscopy (ARPES). In addition to bulk sensitivity the resonant character of the RIXS process also enables mapping of the electronic structure of buried structures and eventually their interfaces. Furthermore, it is worth noting that as a consequence of the involvement of the localized core electron with its well-defined angular symmetry RIXS yields in addition to the $E(k)$ relationship also the local symmetry character of the band states. This is demonstrated in Fig. 3 where we find that states with local p symmetry at the C sites (probed by C K RIXS) dominate the upper part of the VB while states with local s + d symmetry at the Si sites (probed by Si $L_{2,3}$ RIXS) are located in the lower part of the VB.

To summarize, RIXS can be used for detailed band structure mapping of materials with negligible electron-correlation effects. Without any further theoretical input $E(k)$ is mapped around high-symmetry points like the CBM. At other parts of the Brillouin zone the techniques provides a self-consistency test to band structure calculations. As a photon based technique with sufficient bulk sensitivity it should be regarded as a complementary technique to angular resolved photoemission spectroscopy which remains the standard technique for band structure mapping.
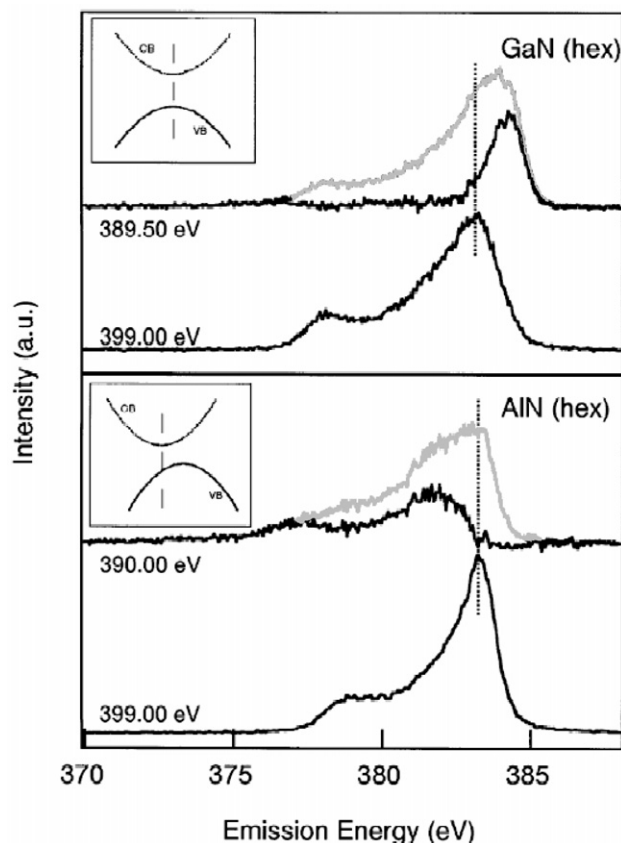
Fig. 2. Comparison of RIXS spectra (upper black curve in each panel) of a direct (GaN, upper panel) and an indirect (AlN, lower panel) band gap material. Non-resonant SXE spectra are given by the lower black curve. The gray curves are the as measured resonantly excited spectra. Figure reproduced from Ref. [20].
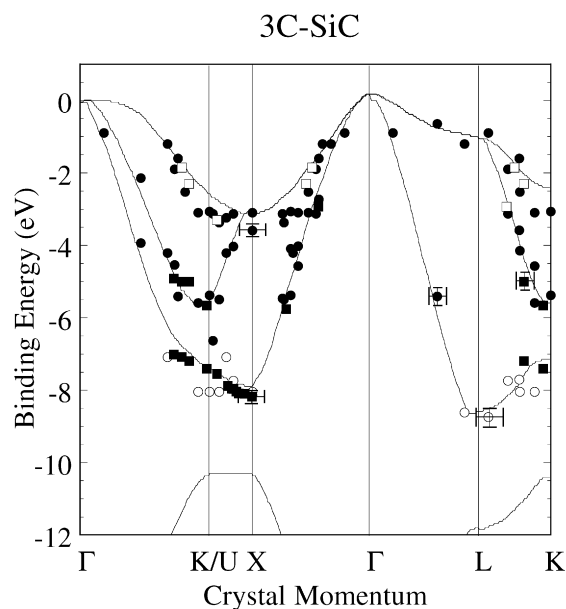

Fig. 3. Comparison of a band structure calculation for cubic SiC [25] with the result of element and symmetry selective band mapping by RIXS [26]. Dots and squares indicate states with local carbon p and silicon s + d character, respectively. Figure reproduced from Ref. [26].

3. RIXS and electron correlations

One of the outstanding issues in modeling real materials is how to treat electron correlations. In the local density approximation (LDA) each electron is independent of all the others. The others are simply represented by their average density. This works very well for many materials and can readily be confronted to the fluorescence X-ray emission i.e. non-resonantly excited X-ray emission (XE) spectra (here we deal with both soft and hard XE). In materials such as the transition metal oxides, electron correlations are at the origin of a whole range of subtle changes in their resistivity, magnetic ordering, and structure as a function of temperature, pressure, or composition. Several theoretical approaches have been made in recent years to account realistically for the electron correlations and presently calculations based on dynamic mean field theory (DMFT) are poised to make a significant contribution to the understanding of highly correlated electron systems such as materials with Mott–Hubbard metal–insulator transitions [27]. It should be noted that DMFT is designed to deal with the more or less degenerate localized electrons but it essentially relies on LDA to describe extended s and p states. RIXS and non-resonant-like XE can play a somewhat analogous role. RIXS measures the electron transfer energy between orbitals, both on-site and between neighboring atoms, e.g. dd excitations correspond to the reorganization of d electrons without changing the total d electron count while charge transfer excitations correspond to the case where the electron count has increased by one following an electron transfer from a neighboring atom. Non-resonant-like XE reflects the occupied densities of states only.

As with X-ray absorption spectroscopy, there remains, however, the difficulty of dealing with the core-hole in the intermediate state as the Coulomb interaction between the core-hole and the excited electron may significantly modify the localization or hybridization in the intermediate state and hence that of the final state.

The single impurity Anderson model as pioneered by A. Kotani (see Ref. [5]) is particularly successful in this respect. A typical application consists in modeling a single transition metal ion so as to be able to account both for the on-site Coulomb interactions and the hybridization with the conduction electrons. To gain more insight into solid state effects it can be extended to more than one transition metal site (periodic Anderson model). On the other hand, it is sometimes possible to neglect hybridization and then to use a truly atomic model. MnO was the subject of the first application of RIXS to dd excitations by Butorin et al. [28] and was interpreted in terms of a purely atomic model. More recent, higher resolution measurements are compared to the single impurity Anderson model [29]. The new experiment confirms the findings by Butorin et al. but it clearly demonstrates that structure arising from charge transfer excitations can only be explained by the single impurity Anderson model.

In what follows we have picked examples that illustrate the use of the technique. At the forefront of the advantages is the bulk and element selectivity of RIXS when dealing with materials which necessarily have to be prepared ex-situ or which may have different surface and bulk properties. Most experiments have concentrated on rare earth or transition metal compounds, especially those related to high temperature superconductors (HTSC) or magnetoresistive materials. They are usually performed at room temperature under vacuum, but where appropriate, temperature dependence is easy to implement and in the harder X-ray region measurements have also been performed under high pressure.

Our first example comes from one of the early RIXS experiments performed on beam line 7.0.1 at the third generation Advanced Light Source. The Uppsala University Nordgren-spectrometer and gas cell were used [30]. The purpose was to study the simplest possible case of d-excitations in a transition metal ion. For that $TiCl_4$ was chosen as it has nominally a d^0 ground state and is liquid at room temperature with a high vapor pressure, making it straightforward to study the gas phase at room temperature [31].

Fig. 4 shows spectra for excitations to three features in the Ti L_3 X-ray absorption spectrum (labeled A, B, and B''). The spectrum of an excitation beyond the L_2 edge at 472 eV (E) is also given on an expanded intensity scale. A small shift is observed in the peak situated at approximately -6 eV (6 eV energy loss) according to whether the excitation is to peak A or B in the absorption spectrum. Excitation to E gives rise to a loss peak at -13 eV. Fig. 4 shows the result of a calculation using the impurity Anderson model corresponding to resonant excitation at A and B.
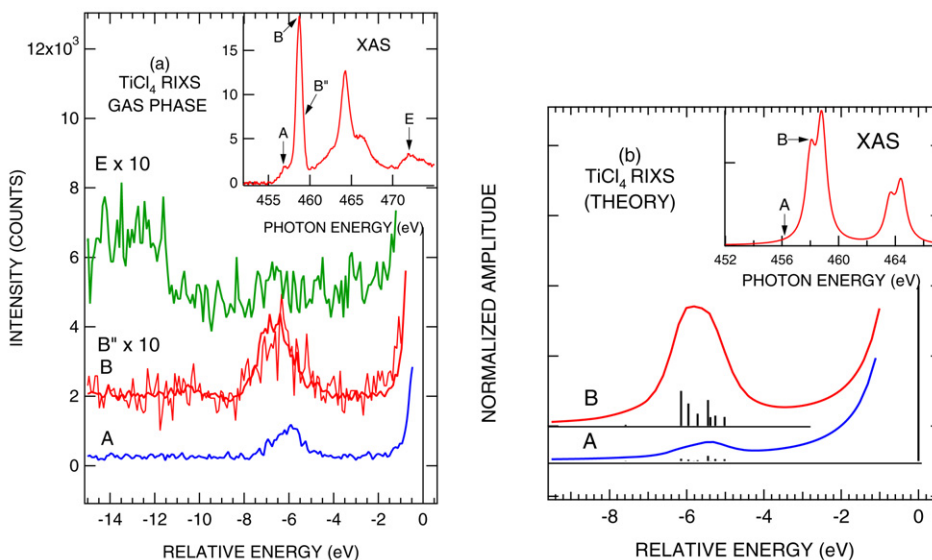

Fig. 4. Ti 2p3d2p RIXS for gas phase $TiCl_4$. Spectra A, B, B'', and E are measured at the excitation energies shown with respect to the XAS data in the inset (a). Calculated RIXS curves using the SIAM approximation (b).
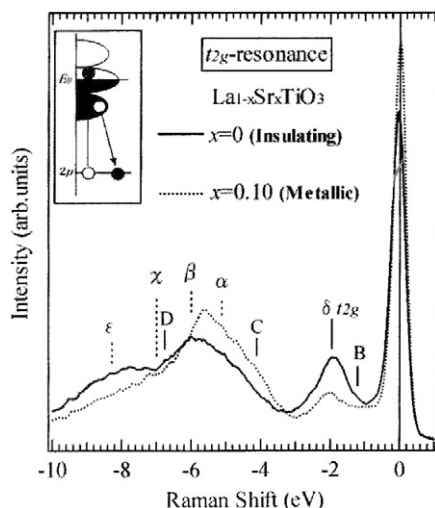
Fig. 5. t_{2g} resonance in LaTiO$_3$ and La$_{0.90}$Sr$_{0.10}$TiO$_3$. After Ref. [32].

The ground state is the bonding state of the 3d^0 and 3d$^1\underline{L}$ configurations where $\underline{L}$ represents a ligand hole, and the final state of the inelastic peak corresponds to the nonbonding 3d$^1\underline{L}$ configuration.

The experimental observation that the excitation energy of the nonbonding state is slightly larger for incident photon energy B and B″ than A is reproduced by the calculation. Thus the origin of this shift is identified as a consequence of symmetry selection of the 3d state: for A and B, the 3d states with E and T$_2$ symmetry are selectively excited in the intermediate state, so that the 3d state probed in the nonbonding 3d$^1\underline{L}$ final state is mainly E or T$_2$, respectively. Continuum states have to be included in the calculation to account for certain of the features such as the −13 eV structure. Thus we see how RIXS can pick out the bonding, nonbonding and antibonding states in such an ionic compound.

We can now move on to the solid state and see how RIXS can contribute to an understanding of the electronic structure in key materials. La$_{0.90}$Sr$_{0.10}$TiO$_3$ is a Mott-Hubbard insulator where Ti can go from a nominally d^0 configuration when $x = 0$, to d^1 when $x = 1$ [32]. Fig. 5 shows the RIXS spectra as a function of the Sr doping and excitation to the t_{2g} resonance of Ti. It should be noted that in the solid state, as opposed to the gas phase, non-resonant-like XE structure is also observed even when the excitation energy is below the ionization threshold (these are labeled from B to D in Fig. 5). Higuchi et al. were able to distinguish between the non-resonant-like XE structure and the Raman-like excitations by recording high resolution spectra in steps across the Ti L$_3$ edge. Non-resonant-like XE is due to the possible escape of the excited electron to neighboring sites, thus making the scattering process independent of the incident photon energy [33,34]. Calculated spectra necessarily need to be based on a cluster of several ions. The Raman shifts (energy losses) are labeled with Greek letters in Fig. 5 where the energy scale is set relative to a specific incident photon energy. The experimental resolution is 0.3 eV which sets the energy limit to the detection of any loss structure. The elastic peak is slightly asymmetric which suggests that even better resolution would reveal lower energy loss features. The Raman peak δ at 2.0 eV corresponds to the dd transition from the lower Hubbard band to the unoccupied quasiparticle band. In this compound there is negligible t_{2g} band splitting so that the contribution to the Raman scattering is due to the on-site electron correlation energy along the lines shown in the inset. From this it is possible to estimate the on-site electron correlation energy ($U_{dd}/2$), and it indicates that U_{dd} is independent of the Sr concentration. It is seen that the intensity of the δ t_{2g} peak in the band gap decreases with Sr doping.

Amongst the many other RIXS experiments based on materials containing a 3d metal, especially Mn and Cu, we would mention those performed at the metal 3p edge [35,36]. They have attracted much attention because of the low binding energy of the 3p shell (∼30–75 eV). It means that, in this energy region, the resolution can be high even with modest resolving power. Spectrometers are being designed to reach a few meV resolution over this energy range [37]. A handicap for experiments in this energy region is the low fluorescence yield, a large contribution from elastic scattering, and small spin-orbit splitting of the 3p levels. On the other hand, RIXS at the Cu L$_3$ edge to study, for example, the important HTSC materials, which requires particularly high resolving power [38], will become available with the next generation of spectrometers (see Section 4).
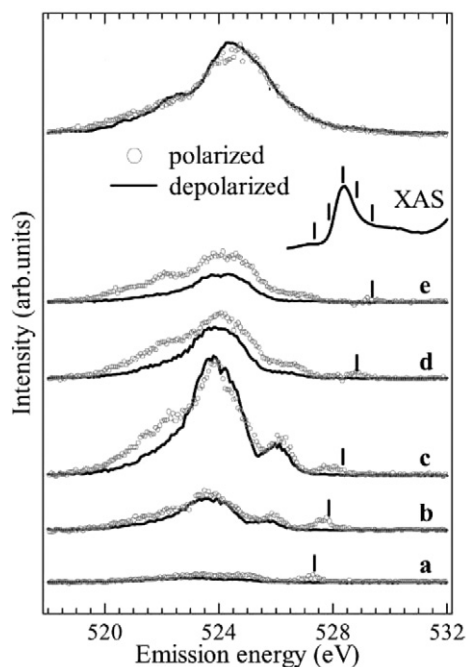
Fig. 6. O 1s Fluorescence XE (top curve) and RIXS for Sr$_2$CuO$_2$Cl$_2$. Letters indicate excitation energies represented by ticks (from left to right) on the O 1s XAS curve (see Ref. [41]).
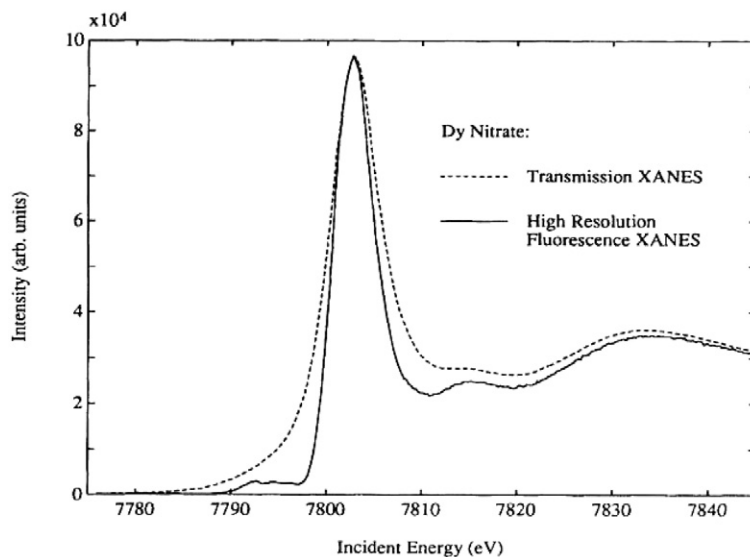
Fig. 7. X-ray absorption near-edge spectrum (XANES) of Dy L$_3$ edge using a narrow energy band of X-ray fluorescence as compared to the transmitted intensity [17].

Where oxides are concerned, another approach consists in measuring the 1s2p1s RIXS at the OK edge. Duda et al. [39] showed that, because of hybridization between the O 2p and Cu 3d states it is possible to use the O 1s resonances to obtain information concerning the dd excitations as well. Such an experiment was performed on CuGeO$_3$ which has edge sharing CuO$_4$ units and shows an energy loss structure of ∼2 eV. The loss structure is attributed to a Zhang Rice singlet (ZRS). In this process a Cu 3d hole is transferred to a neighboring Cu site as a consequence of the O 1s core-hole excitation (1s excitation to hybridized-2p states in the intermediate state). Okada and Kotani [40] presented a model calculation confirming this interpretation and predicted that the symmetry selective properties of polarized photons could be used to confirm the origin of such a feature. Indeed, the anisotropy at the O site is large in the low dimensional cuprates. Experiments subsequently performed on Sr$_2$CuO$_2$Cl$_2$ (see Fig. 6) [41] did show a polarization dependence of the ZRS intensity, though the dependence is apparently smaller than predicted. Modeling the O 1s2p1s RIXS has the advantage that the core-hole–valence-electron Coulomb interaction is small and can generally be neglected in the calculations.

Interactions between the 4f electrons and the valence states of rare earths or the other constituents of a compound have been explored for many decades. Of particular interest are Ce at the beginning and Yb at the end of the series because of their rich mixed valent properties. In RIXS, 4f states may be reached via normal dipole selection rules from the 3d or 4d core levels; the corresponding decay channels are then in the soft X-ray energy region. They can also be reached via quadrupole transitions from the 2p core-levels. These quadrupole transitions are of interest in their own right and many experiments have been performed which monitor the 3d → 2p decay channel while exciting the rare earth L edge. The probability of a 2p → 4f transition is weak and the dominant component in the absorption spectrum is 2p → 5d. Even so, a weak pre-edge feature has been observed in several of the rare earth absorption edges when experiments are performed under high resolution conditions.

The most discussed experiment of this kind is that described by Hämäläinen et al. [17]. They measured the Dy L$_3$ X-ray absorption edge (see Fig. 7) by monitoring the intensity of the 3d → 2p radiative decay channel within a narrow energy band centered on the Lα_1 line. In this experiment, performed at NSLS (Brookhaven), the energy resolution was $\Delta E_{in} = 0.7$ eV for the incident photons at 7.8 keV and $\Delta E_{out} = 0.3$ eV for the detected photons at 6.5 keV. Under these conditions a well-defined pre-edge structure, not observed in a normal X-ray absorption spectrum, becomes
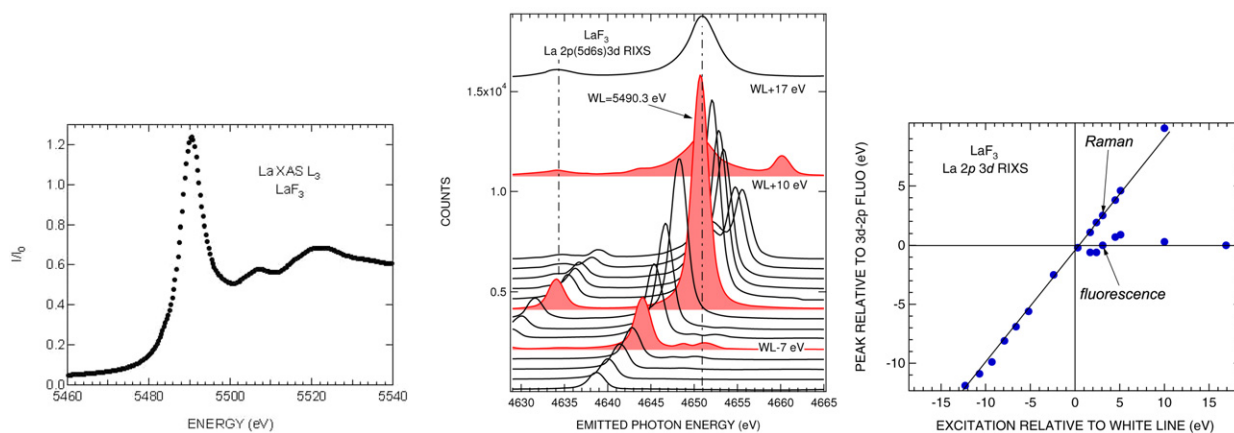
Fig. 8. La L_3 in LaF$_3$ XAS (left panel) peaks at 5490.3 eV. La 2p(5d6s)3d RIXS (center panel) reaches maximum intensity at the white line energy (WL). Other spectra are measured below and above WL. A double peak structure resonates at WL-7 eV. Raman and fluorescence regimes are plotted (right panel).

apparent. This experiment was widely judged to be a breakthrough for performing high resolution X-ray absorption measurements. The interpretation was contested, however, by Carra et al. [18] who showed that a more extensive data set was needed if a valid undistorted description of the electronic structure was to be gained. The pre-edge structure was attributed to 2p–4f quadrupole transitions which can be calculated quite precisely within an atomic model because of the localized nature of the 4f states. It is to be noted on the other hand that the 2p to 5d6s excitations can only be dealt with in a phenomenological manner because of the band-like nature of the valence/conduction states. The first experiment along the lines proposed by Carra et al. was performed by Krisch et al. [42] on the Gd L_3-edge. In Fig. 8 we present an equivalent set of data for the La L_3-edge in the ionic LaF$_3$ compound (see Ref. [43]). LaF$_3$ has a $4f^0(5d6s)^0$ configuration which makes it somewhat equivalent to the TiCl$_4$ case with its nominally $3d^0$ configuration.

In Fig. 8 the incident photon energy has been incremented in steps of ∼1.5 eV. The main peak, which involves the $2p_{3/2} \rightarrow 5d$ excitation, is seen to disperse regularly as the incident photon energy is increased up to the maximum (white line) of the absorption spectrum. As the white line (WL) is reached the RIXS spectrum splits into two components. One continues to disperse but its intensity gradually weakens, while the other, corresponding to a fluorescence-like emission remains at almost constant energy. This behavior indicates that two processes coexist: there is an excitonic coupling of the 2p hole and the 5d electron in the intermediate state which explains the dispersing feature, but the excited electron may also decay to a neighboring site leading to a non-resonant-like decay of the 2p core hole [44]. We observe the quadrupole structure quite clearly thanks to its resonant enhancement 7 eV before reaching the absorption maximum. It means that the 4f electron screens the core-hole more efficiently than a 5d electron and that the energy difference corresponds to the difference between the energies of their Coulomb interactions $(U_{cf} - U_{cd})$. The double peak arises from the interaction between the single 4f electron and the 3d core-hole in the final state (see Refs. [34,45]).

Fig. 9 shows that if the same experiment is performed on an alloy such as LaPd$_3$ where the La 5d6s states hybridize with the transition metal d states (here Pd 4d states) then the intensity of the structure, previously identified as 4f states and reached via a quadrupole transition, increases significantly. It suggests that this time the same excited state is reached via a dipole transition resulting from an interaction between the 5d valence states and 4f electrons. The cross section for quadrupole transitions is small and the ratio of the amplitude of peak B on resonance to the amplitude of the 2p5d dipole transition on resonance at the X-ray absorption maximum is for LaF$_3$ ∼1 : 40. The equivalent ratio in LaPd$_3$ is ∼1 : 6.5. This indicates that the 4f states do mix with the conduction states and are a clue to the origin of the mixed valent properties of many of the rare earth elements.

We can also use Fig. 8 to illustrate the difference between the Hämäläinen et al. experiment and a full RIXS data set. As already mentioned the former consists in fixing the observation to a narrow energy band in the vicinity of the Lα_1 XE peak, here at 4651 eV, as the incident photon energy is incremented. Clearly the XAS spectrum would miss some of the detail that can be extracted from the full RIXS data set. From this it is clear that Carra et al. [19] were right to challenge the validity of the Dy L_3 experiment. However, by suppressing the lifetime broadening of the intermediate
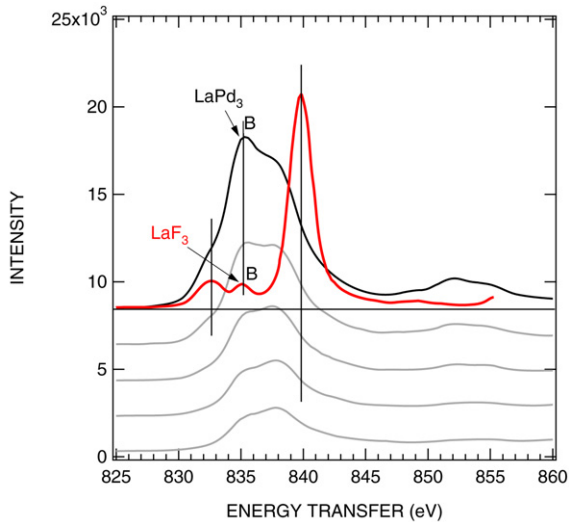
Fig. 9. Double peak structure in the RIXS spectra taken 7 eV below the La L_3 edge in LaF_3 and in La Pd_3 showing the change in intensity as a result of alloying (spectra are normalized relative to the respective RIXS data taken at the WL maximum and plotted here on an energy transfer scale).
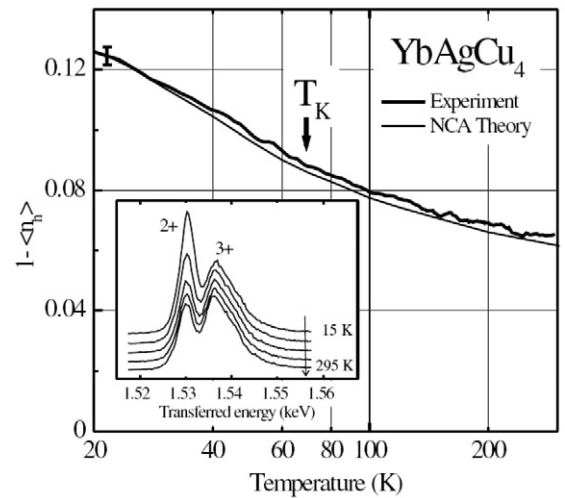
Fig. 10. Temperature dependence of the Yb^{2+} RIXS signal for $YbAgCu_4$, in good agreement with the predicted Kondo scaling according to [46].

core-hole state, it provides a means of spotlighting weak features otherwise unobservable in the absorption spectrum. Full RIXS on the other hand provides new information on the degree of localization of the 4f electrons, a subject that has been debated for many years. The suppression of the intermediate-state lifetime broadening is a consequence of energy conservation. The small excitation and observation energy bandpass, together with the small final state core-hole broadening limit the total width to the convolution of the three functions.

Recently Dallera et al. [46] were able to make a quantitative assessment of the 4f counts in two Yb alloys which are well described by the Anderson impurity model, namely, $YbInCu_4$ and $YbAgCu_4$. The former alloy has a sharp change in the f-electron count at a transition temperature of 42 K whereas the latter has a continuous change in the 4f count as a function of temperature as demonstrated by the RIXS measurements shown in Fig. 10. The spectra were measured in the Yb L_3 pre-edge region which is associated with the 4f occupancy. They showed that the temperature variation of the Yb^{2+} peak is in accordance with the predicted Kondo scaling.

Rueff et al. [47] have studied the Ce γ–α phase transition of Ce under pressure. In the latter case metallic Ce is placed in a high pressure cell and the scattered X-rays are measured through a Rh gasket. The RIXS spectrum under a pressure of 1.5 kbar is barely different from that at ambient pressure. However, a striking increase (∼40%) in the $4f^2/4f^1$ intensity ratio is observed as the system passes the γ–α transition under pressure with the accompanying 15% change in volume. Measurements were compared to a full multiplet calculation within the Anderson impurity model. The increased contribution from the $4f^2$ component at high pressure revealed by the RIXS data is accompanied by an increase in intensity for another structure observed more clearly in the XAS data that corresponds to a $4f^0$ component. This stresses the growing interaction between 4f and conduction electrons which is a characteristic feature of a Kondo-like behavior. The growth of double occupancy at low volume points to less correlation in the α phase as electron hopping is favored. There is thus a coexistence of competing effects: partial delocalization of the 4f electrons through band formation with the conduction states, on the one hand, and reduced electron–electron correlations that allows the system to accommodate stronger on-site repulsion, on the other hand.

Another major contribution to the electronic properties of materials science made by RIXS in the hard X-ray regime is provided by the use of the momentum-dependent information concerning charge excitations. We take La_2CuO_4, the parent material of the HTSC's, as an example. Fig. 11 shows the dependence of energy loss features observed in the Cu 1s4p1s RIXS where q is parallel to the $\langle 110 \rangle$ (0, 0 to π, 0) or $\langle 100 \rangle$ (0, 0 to π, π) direction [48]. The energy loss in such a RIXS experiment corresponds schematically to the excitation of an electron from the lower Hubbard band (LHB) to the upper Hubbard band (UHB). The dispersion of the LHB is known from angle resolved photoemission
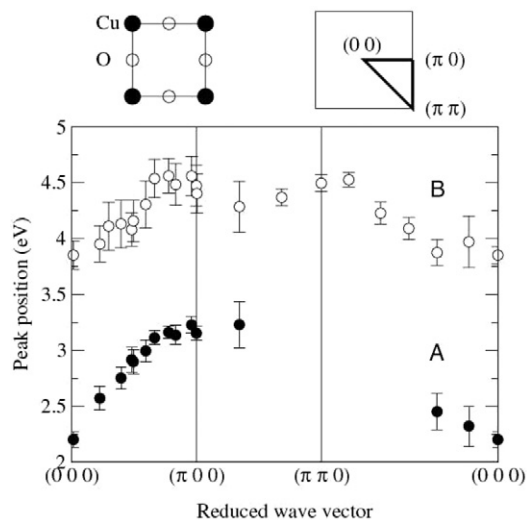
Fig. 11. The peak positions of two features observed in the 1s4p1s RIXS spectrum are plotted along the high symmetry directions of the Brillouin zone as shown schematically in the top panel [48].

spectroscopy, and to map the dispersion of the UHB the variable momentum transfer is achieved by varying the scattering angle relative to the incident photon direction. At the K edge the wavelength of the excitation is in the one Å range so that it is possible to scan a large portion of the Brillouin zone. At the center of the Brillouin zone, the energy losses in the example chosen are 2.2 eV and 3.9 eV with a dispersion of about 1 eV and 0.5 eV, respectively (see Fig. 11). It was argued that these are both highly dispersive exciton-like modes, strongly damped by the presence of the electron-hole continuum. On the other hand, Nomura and Igarashi [49] attribute the two-peak feature to the fine structure of the Cu 3d partial density of states mixed with the O 2p band. A detailed discussion can be found in Refs. [34,50].

4. X-ray spectrometers

Designing X-ray spectrometers differs from X-ray monochromators for synchrotron radiation. Synchrotron radiation has high emittance within a small cone, especially in the context of an undulator beam line, whereas the secondary emission from a target is essentially isotropic over a sphere of 4π radians. In the hard X-ray region energy dispersion can be obtained using crystals and applying Bragg's law. The latter imposes $\lambda < 2d\sin(\theta)/m$ where λ is the wavelength of the photons, d the crystal lattice spacing, θ the Bragg angle and m is the order of diffraction. Wavelength (or energy) dispersion is greatest when $\theta \to 90°$. Beryl crystals have a $2d$ of 1.6 nm which is the highest value available for high resolution experiments. Thus in effect the limiting condition for the use of crystal spectrometers is $\lambda < 1.6$ nm ($E > 770$ eV). The resolving power at the L edge of Cu can attain $\sim$2000 [51]. The general goal is therefore to use well focused beams to create a small secondary source on a Rowland circle; to select d and m to obtain a Bragg condition with a large value of θ and collect a large portion of the solid angle by using a large spherically-bent crystal. The diffracted beam can then be measured with an appropriate detector such as a photodiode as the small size of the source serves the purpose of an entrance slit.

In the hard X-ray region much of the optical path can be in air thus greatly facilitating the construction of spectrometers with large dimensions. The scattering angle of the photons can be chosen to satisfy the quantum transfer conditions needed to scan the Brillouin zone of the sample. Even under resonance conditions, 1s4p1s RIXS for instance, the counting rates are of only a few counts per minute. As a consequence spectrometers are being fitted with large arrays of spherical crystals so as to intercept 1% or more of the total radiation.

In the soft X-ray range, gratings are used. The grating formula is $m\lambda = d(\cos\alpha - \cos\beta)$ where α and β are the grazing incidence and reflected angles respectively measured from the plane of the grating. The practical technological limit to groove spacing is of the order of 280 nm corresponding to a line density of 3600 l/mm. The reflectivity in the soft X-ray region is low except for small grazing angles. In practical terms, this has to be less than $\sim$3° in the 300 eV

to 700 eV region even for coatings with the highest reflectivity and smaller still above 700 eV. This dramatically reduces the solid acceptance angle intercepted by the instrument.

The parameter α can be fixed and a 2D detector can be used to collect simultaneously a whole range of wavelengths (βs). In this case the most efficient geometry consists in using a very well focused primary beam in place of a larger source limited by a slit. To date the most widely used X-ray spectrometer is that designed by Nordgren et al. [52] which uses ruled or holographically prepared laminar gratings with a constant pitch placed in a Rowland mounting and a 2D position sensitive detector. The image suffers from a strong curvature, but this can be corrected by using computer analysis. Because of its compact dimensions, the solid angle intercepted is relatively large but the resolving power limited to, at best, 1500. Other instruments use varied line spacing gratings [53] that implement Fermat's principle to reduce image aberrations or even obtain a flat field image. Now that it is recognized that RIXS is one of the techniques that will benefit most from the latest developments in synchrotron radiation facilities, beam lines are being built that meet its specific requirements: very high flux and small focus such as the Microfocus beam line at SOLEIL and Adress at SLS. To meet the new challenge new spectrometers are being commissioned [54,55] or are at the design stage [56] with ultimate resolving powers in the order of 5000 to 10000 and an extended energy range.

References

[1] W. Eberhard, J. Lüning, J.-E. Rubensson (Eds.), Proceedings of the International Workshop on Resonant Inelastic Soft X-Ray Scattering in Walberberg, Appl. Phys. A 65 (1997) 89–194.
[2] E.Z. Kurmaev, J. Nordgren (Eds.), Soft X-Ray Emission Spectroscopy, J. Elec. Spec. Rel. Phen. 110 (2000).
[3] G. Materlik, C.J. Sparks, K. Fischer (Eds.), Resonant Anomalous X-Ray Scattering: Theory and Applications, North-Holland, Amsterdam, 1994.
[4] P.M. Platzman, E.D. Isaacs, Phys. Rev. B 57 (1998) 11107.
[5] A. Kotani, S. Shin, Rev. Mod. Phys. 73 (2001) 203.
[6] J.P. Briand, D. Girard, V. Kostroun, P. Chevallier, K. Wohrer, J.P. Mossé, Phys. Rev. Lett. 46 (1981) 1625.
[7] H.W.B. Skinner, Rep. Prog. Phys. 5 (1938) 257.
[8] E.g., R.H. Williams, G.P. Srivastava, I.T. McGovern, Photoelectron spectroscopy of solids and their surfaces, Rep. Prog. Phys. 43 (1980) 1357.
[9] J. Nordgren, G. Bray, S. Cramm, R. Nyholm, J.-E. Rubensson, N. Wassdahl, Soft X-ray emission spectroscopy using monochromatized synchrotron radiation, Rev. Sci. Instrum. 60 (1989) 1690.
[10] J.-E. Rubensson, D. Mueller, R. Shuker, D.L. Ederer, C.H. Zhang, J. Jia, T.A. Callcott, Phys. Rev. Lett. 64 (1990) 1047.
[11] J.-E. Rubensson, J. Lüning, S. Eisebitt, W. Eberhardt, It's always a one-step process, Appl. Phys. A 65 (1997) 91 and references therein.
[12] J.J. Sakurai, Advanced Quantum Mechanics, Addison–Wesley, London, 1967.
[13] N. Mårtensson, M. Weinelt, O. Karis, M. Magnuson, N. Wassdahl, A. Nilsson, J. Stöhr, M. Samant, Appl. Phys. A 65 (1997) 159.
[14] S. Eisebitt, W. Eberhardt, J. Elec. Spec. Rel. Phen. Rel. Phen. 110 (2000) 335.
[15] P. Skytt, P. Glans, J.-H. Guo, K. Gunnelin, C. Såthe, J. Nordgren, F. Gel'mukhanov, A. Cesar, H. Ågren, Phys. Rev. Lett. 77 (1996) 5035.
[16] M. Simon, L. Journel, R. Guillemin, W.C. Stolte, I. Minkov, F. Gel'mukhanov, P. Salek, H. Ågren, S. Carniato, R. Taïeb, A.C. Hudson, D.W. Lindle, Phys. Rev. A 73 (2006) 020706(R).
[17] K. Hämäläinen, D.P. Siddons, J.B. Hastings, L.E. Berman, Phys. Rev. Lett. 74 (1991) 2850.
[18] P. Carra, M. Fabrizio, B.T. Thole, Phys. Rev. Lett. 74 (1995) 3700.
[19] Y. Ma, N. Wassdahl, P. Skytt, J. Guo, J. Nordgren, P.D. Johnson, J.-E. Rubensson, T. Boske, W. Eberhardt, S.D. Kevan, Phys. Rev. Lett. 69 (1992) 2598.
[20] S. Eisebitt, J. Lüning, J.-E. Rubensson, A. Karl, W. Eberhardt, Phys. Stat. Sol. B 215 (1999) 803.
[21] J.A. Carlisle, E.L. Shirley, E.A. Hudson, L.J. Terminello, T.A. Callcott, J.J. Jia, D.L. Ederer, R.C.C. Perera, F.J. Himpsel, Phys. Rev. Lett. 74 (1995) 1234.
[22] A. Agui, S. Shin, M. Fujisawa, Y. Tezuka, T. Ishii, Y. Muramatsu, O. Mishima, K. Era, Phys. Rev. B 55 (1997) 2073.
[23] D. Eich, O. Fuchs, U. Groh, L. Weinhardt, R. Fink, E. Umbach, C. Heske, A. Fleszar, W. Hanke, E.K.U. Gross, C. Bostedt, T. van Buuren, N. Franco, L. Terminello, M. Keim, G. Reuscher, H. Lugauer, A. Waag, Phys. Rev. B 73 (2006) 115212-1-6.
[24] E.L. Shirley, J. Elec. Spec. Rel. Phen. 110 (2000) 305.
[25] S. Logothetidis, H.M. Polatoglou, J. Petalas, D. Fuchs, R.L. Johnson, Physics B 185 (1993) 389.
[26] J. Lüning, J.-E. Rubensson, C. Ellmers, S. Eisebitt, W. Eberhardt, Phys. Rev. B 56 (1997) 13147.
[27] A. Georges, G. Kotliar, W. Krauth, M.J. Rozenberg, Rev. Mod. Phys. 68 (1996) 13.
[28] S.M. Butorin, J.H. Guo, M. Magnuson, P. Kuiper, J. Nordgren, Phys. Rev. B 54 (1996) 4405.
[29] G. Ghiringhelli, M. Matsubara, C. Dallera, F. Fracassi, A. Tagliaferri, N.B. Brookes, A. Kotani, L. Braicovich, Phys. Rev. B 73 (2006) 035111.
[30] J.-H. Guo, N. Wassdahl, P. Skytt, S.M. Butorin, L.-C. Duda, C.J. Englund, J. Nordgren, Rev. Sci. Instrum. 66 (1995) 1561.
[31] C.F. Hague, M. Tronc, Y. Yanagida, A. Kotani, J.H. Guo, C. Såthe, Phys. Rev. A 66 (2000) 012511.
[32] T. Higuchi, D. Baba, T. Takeuchi, T. Tsukamoto, Y. Taguchi, Y. Tokura, A. Chainani, S. Shin, Phys. Rev. B 68 (2003) 104420.
[33] T. Ide, A. Kotani, J. Phys. Soc. Jpn. 7 (1998) 3621.
[34] A. Kotani, Eur. Phys. J. B 47 (2005) 3.
[35] P. Kuiper, J.-H. Guo, C. Såthe, L.-C. Duda, J. Nordgren, J.J. Pothuizen, F.M.F. de Groot, G.A. Sawatzky, Phys. Rev. Lett. 80 (1998) 5204.

[36] S.G. Chiuzbaian, G. Ghiringhelli, C. Dallera, M. Grioni, P. Amann, X. Wang, L. Braicovich, L. Patthey, Phys. Rev. Lett. 95 (2005) 197402.
[37] Y.-D. Chuang, J. Pepper, W. McKinney, Z. Hussain, E. Gullikson, P. Batson, D. Qian, M.Z. Hasan, J. Phys. Chem. Solids 66 (2005) 2173.
[38] G. Ghiringhelli, N.B. Brookes, E. Annese, H. Berger, C. Dallera, M. Grioni, L. Perfetti, A. Tagliaferri, L. Braicovich, Phys. Rev. Lett. 92 (2004) 117406.
[39] L.-C. Duda, J. Downes, C. McGuinness, T. Schmitt, A. Augustsson, K.E. Smith, G. Dhalenne, A. Revcolevschi, Phys. Rev. B 61 (2000) 4186.
[40] K. Okada, A. Kotani, Phys. Rev. B 65 (2002) 144530.
[41] Y. Harada, K. Okada, R. Eguchi, A. Kotani, H. Takagi, T. Takeuchi, S. Shin, Phys. Rev. B 66 (2002) 165104.
[42] M.H. Krisch, C.C. Kao, F. Sette, W.A. Caliebe, K. Hämäläinen, J.B. Hastings, Phys. Rev. Lett. 74 (1995) 4931.
[43] L. Journel, J.-M. Mariot, J.-P. Rueff, C.F. Hague, G. Krill, M. Nakazawa, A. Kotani, A. Rogalev, F. Wilhelm, J.-P. Kappler, G. Schmerber, Phys. Rev. B 66 (2002) 45106.
[44] F. Gel'mukhanov, H. Ågren, Phys. Rev. B 57 (1998) 2780.
[45] M. Nakazawa, K. Fukui, H. Ogasawara, A. Kotani, C.F. Hague, Phys. Rev. B 66 (2002) 113104.
[46] C. Dallera, M. Grioni, A. Shukla, G. Vank, J.L. Sarrao, J.-P. Rueff, D.L. Cox, Phys. Rev. Lett. 88 (2002) 196403.
[47] J.-P. Rueff, J.-P. Itié, M. Taguchi, C.F. Hague, J.-M. Mariot, R. Delaunay, J.-P. Kappler, N. Jaouen, Phys. Rev. Lett 96 (2006) 237403.
[48] Y.J. Kim, J.P. Hill, C.A. Burns, S. Wakimoto, R.J. Birgeneau, D. Casa, T. Gog, C.T. Venkataraman, Phys. Rev. Lett. 89 (2002) 177023.
[49] J. Igarashi, T. Nomura, M. Takahashi, Phys. Rev. B 74 (2006) 245122.
[50] Y.-J. Kim, J.P. Hill, S. Komiya, Y. Ando, D. Casa, T. Gog, C.T. Venkataraman, Phys. Rev. B 70 (2004) 094524.
[51] J.-M. Mariot, M. Sacchi, L. Journel, J.-J. Gallet, M. McElfresh, C.F. Hague, Nucl. Instrum. Meth. Phys. Res. A 246 (2006) 176.
[52] J. Nordgren, G. Bray, S. Cramm, R. Nyholm, J.-E. Rubensson, N. Wassdahl, Rev. Sci. Instrum. 60 (1989) 1690.
[53] T. Harada, T. Kita, M. Itou, H. Taira, A. Mikuni, Nucl. Instrum. Meth. Phys. Res. A 226 (1986) 272.
[54] G. Ghiringhelli, A. Piazzalunga, C. Dallera, G. Trezzi, L. Braicovich, T. Schmitt, V.N. Strocov, R. Betemps, L. Patthey, X. Wang, M. Grioni, Rev. Sci. Instrum. 77 (2006) 113108.
[55] T. Tokushima, Y. Harada, H. Ohashi, Y. Senba, S. Shin, Rev. Sci. Instrum. 77 (2006) 63107.
[56] A very high resolution spectrometer is under construction for the SOLEIL Microfocus Beamline based on the flat field design presented by C.F. Hague, J.H. Underwood, A. Avila, R. Delaunay, H. Ringuenet, M. Marsi, M. Sacchi, Rev. Sci. Instrum. 76 (2005) 23110.